Article:
Tominaga, Shoji, Guarnera, Giuseppe Claudio and Ohtera, Ryo (2026) Spectral Image Rendering of Fluorescent Objects Using a Conventional Renderer. IEEE Transactions on Visualization and Computer Graphics. pp. 5457-5469. ISSN: 1077-2626

https://doi.org/10.1109/TVCG.2026.3668980

Spectral Image Rendering of Fluorescent Objects Using a Conventional Renderer

Life Fellow, IEEE, Shoji Tominaga, Giuseppe Claudio Guarnera, Ryo Ohtera

***Abstract*—We propose a practical spectral image rendering method for fluorescent objects using a renderer that does not natively support wavelength-shifting transport. For scenes composed of matte fluorescent and non-fluorescent surfaces, the illumination incident on a target fluorescent object is classified into three types: (1) direct illumination from a light source, (2) indirect illumination reflected from other reflective objects, and (3) luminescent illumination emitted from other fluorescent objects. We express the radiance observed on a fluorescent surface as a linear combination of five terms: reflection and fluorescence under direct illumination, reflection and fluorescence under indirect illumination, and reflection induced by luminescent illumination emitted by other fluorescent surfaces. Assuming isotropic emission and single-bounce fluorescence, the fluorescent shading terms reuse the diffuse-reflection shading produced by the renderer, while measured Donaldson matrices provide the wavelength conversion. Mitsuba is used as the underlying conventional rendering system. Experiments conducted with a physically built Cornell Box validate the proposed method through comparisons with direct measurements and an existing fluorescence-capable renderer. Finally, we demonstrate an extension to non-planar fluorescent objects via sparse emitter discretization.**

***Index Terms*—Fluorescence, Spectral Image Rendering, Non-Fluorescence-Aware Renderer.**

I. INTRODUCTION

MANY objects around us are reflective, with optical characteristics determined by their surface spectral reflectance in the visible wavelength range of 400-700 nm. However, reflectance alone does not fully characterize all materials. Many common materials also exhibit fluorescence, a wavelength-shifting phenomenon in which a material absorbs light in an excitation band and re-emits it at longer wavelengths [1], [2]. Fluorescent agents are widespread in everyday objects—paper, paints, plastics, and textiles—as well as in natural materials such as minerals and plants. Fluorescence can strongly affect appearance, often increasing perceived brightness and saturation, making accurate fluorescence modeling essential for physically based rendering.

Conventional approaches to physically based fluorescence rendering require a fluorescence-aware spectral renderer that explicitly samples wavelength-shifting events along light-transport paths. In this paper, we show that, under standard assumptions for matte fluorescent materials, a conventional (non-fluorescence-aware) spectral renderer can be repurposed to synthesize fluorescent scenes *without modifying* its light-transport core.

S. Tominaga is with the Department of Computer Science, Norwegian University of Science and Technology, 2815 Gjovik, Norway, and the Department of Business and Informatics, Nagano University, Ueda 386-1298, Japan.

G. C. Guarnera is with the Department of Computer Science, University of York, York, United Kingdom

R. Ohtera is with the Kobe Institute of Computing, Graduate School of Information Technology, Chuo-ku, Kobe 650-0001, Japan

Figure 1: Color image of the Cornell Box rendered in this study.

To achieve this, we make two assumptions about fluorescence. First, our spectral model for mutual illumination between fluorescent object surfaces is based on single bounce (path length 2) between two objects; that is, the fluorescence emission occurs only once and does not recur. In other words, the luminescent illumination emitted from a fluorescent object does not excite other fluorescent objects. Second, we assume that the spectral radiance of a three-dimensional fluorescent object can be factored into a product of spectral functions (such as spectral reflectance, luminescence spectra, and scene illuminant) and shading terms (related to object geometry, texture, and the positions of the light source and camera). The spectral functions are inherent to each fluorescent material and illuminant, while the shading terms change with the object's shape, viewpoint and light source position. We further assume Lambertian surface reflection and approximately isotropic fluorescent emission [23], [24]. Building upon the similarities between diffuse reflection and fluorescent emission, we show that the shading terms for the fluorescent components can be obtained from those of the reflection components. Consequently, the spectral image of a fluorescent object can be synthesized using a standard renderer. Tominaga et al. [15] proposed an approach for the appearance synthesis of two closely placed fluorescent objects with matte surfaces under uniform illumination.

Here, we further extend this approach to general scenes, in which multiple objects, including fluorescent objects with matte surfaces, are present and may not be uniformly illuminated. We use the Cornell Box as a test environment, which is a well-known benchmark for assessing the accuracy of rendering systems by comparing rendered scenes with real observations [16]–[18]. Figure 1 shows a color image of the Cornell Box rendered in this study. The surface geometry and location of each object follow the original data available at [19]. The red and green walls on the sides are fluorescent. The light source is CIE standard illuminant D65 [1]. The remaining walls, ceiling, floor, and the two gray rectangular objects are matte and non-fluorescent, and their spectral reflectances were taken from the real object.

Motivation for using a conventional renderer.: Our decomposition allows us to reuse standard diffuse-shading terms to synthesize single-bounce fluorescence from measured Donaldson matrices in a renderer that lacks native wavelength-shifting transport. This approach improves *portability* and *interpretability*, as each of the five components can be rendered and inspected, while keeping the renderer's native evaluation on non-fluorescent surfaces unchanged. Limitations are summarized in Section VIII-A.

The remainder of this paper is organized as follows. Related work is summarized in Section II. In Section III, we describe the bispectral model of a fluorescent object and define the Donaldson matrix. In Section IV, we present the spectral image formation process and derive the five-component decomposition. In Section V, we describe the computation of each component using Mitsuba V0.6 [20]. Section VI reports validation on a real Cornell Box and comparisons with an existing spectral render that supports fluorescence (the Advanced Rendering Toolkit - ART [21]). Finally, Section VII generalizes the method to non-planar fluorescent objects.

II. Related Work

Fluorescence characterization and Donaldson matrices: Fluorescent behavior is commonly encoded by the bispectral radiance factor—also called the Donaldson matrix—which describes how incident wavelengths are re-emitted at (typically longer) wavelengths, independent of the illuminant [2], [3]. A series of imaging approaches estimate Donaldson matrices or their factorizations from multispectral captures under multiple illuminants. In particular, Tominaga et al. proposed practical acquisition and estimation pipelines for matte surfaces that recover the full matrix or compact factorizations from a small number of illuminations and sensor channels [5]–[7], [15], [29]. These methods provide bispectral inputs suitable for predictive rendering and for validating renderer output.

Bispectral models and measurements: The Bispectral Bidirectional Reflectance and Reradiation Distribution Function (BBRRDF) extends the BRDF to wavelength-shifting phenomena. Hullin et al. [4] acquired and analyzed full BBRRDFs for several fluorescent materials and introduced a PCA-guided strategy to reduce measurement time while retaining angular dependence. Earlier, Wilkie et al. [11] introduced an analytic reflectance model for diffuse fluorescent surfaces based on a layered microfacet construction, which couples a conventional reflectance lobe with a diffuse fluorescent component parameterized by a reradiation matrix. More recently, Jung et al. [12] proposed a simple, analytical, purely diffuse BBRRDF that is continuous in wavelength and parameterized by absorption and emission spectra together with a base reflectance; they discuss energy and photon conservation and provide direct sampling of incident and exitant wavelengths.

Rendering algorithms with fluorescence: Supporting fluorescence in physically based renderers requires spectral transport with wavelength-shifting events. Wilkie et al. [10] demonstrated combined rendering of polarization and fluorescence in a spectral Monte-Carlo renderer using reradiation matrices defined over discrete bands. Mojzík et al. [13] extended hero-wavelength spectral path tracing to handle fluorescent events on surfaces and in volumes and proposed a distance-tracking scheme for strongly asymmetric fluorescent volumes. More recently, Jung et al. [14] introduced spectral mollification to enable bidirectional connections in the presence of fluorescence, permitting bidirectional spectral path tracing; they also discuss that the regularization changes the evaluation at non-fluorescent surfaces, which must be considered when interpreting color accuracy.

Compact representations and sampling: A practical bottleneck for bispectral rendering is the memory and sampling cost of Donaldson matrices. Hua et al. represented reradiation matrices by compact two-dimensional Gaussian mixtures and sampled wavelength-shifting events from the conditional mixture, achieving large memory savings while maintaining accuracy; they demonstrated seamless integration into a standard Monte Carlo path tracer and quantitative comparisons on measured datasets [8]. Such compact representations are complementary to our design: they can be used as inputs to further reduce overhead when adapting a non-fluorescence-aware renderer to fluorescent materials.

In contrast to prior work that either acquires full bispectral data or relies on renderers with native bispectral transport, we adapt a conventional (non-fluorescence-aware) renderer by factorizing spectral and shading terms to model single-bounce luminescent transport, reusing reflection shading and remaining compatible with measured Donaldson matrices, bridging the gap between the works above and practical pipelines.

III. Bispectral model of a fluorescent object

Let the Donaldson matrix be represented as a two-variable function $D(\lambda_{em}, \lambda_{ex})$ that depends on the excitation wavelength λ_{ex} and the emission (or reflection) wavelength λ_{em}. The excitation wavelength for many fluorescent materials typically starts from approximately 330 nm to 350 nm [22]. In this study, due to the operating range of the spectral renderer, the excitation range is set to $360\,nm \leq \lambda_{ex} \leq 700\,nm$, thereby including parts of the near-UV and visible wavelengths. In contrast, because common imaging systems operate in the visible wavelength range for the human visual system, the emission and reflection range is set to $400\,nm \leq \lambda_{em} \leq 700\,nm$.

The Donaldson matrix is decomposed into two components: the reflected radiance factor $D_{\mathrm{R}}(\lambda_{em}, \lambda_{ex})$ associated with light reflection, and the luminescent radiance factor $D_{\mathrm{L}}(\lambda_{em}, \lambda_{ex})$ associated with fluorescent emission. The matrix $D_{\mathrm{R}}(\lambda_{em}, \lambda_{ex})$ is diagonal and has nonzero entries only when $\lambda_{em} = \lambda_{ex}$, corresponding to the surface spectral reflectance $S(\lambda)$. The matrix

$D_\mathrm{L}(\lambda_{em}, \lambda_{ex})$ contains off-diagonal values with $\lambda_{em} > \lambda_{ex}$ due to the Stokes shift (see [2]). Assuming that a fluorescent object contains a single fluorescent chemical compound, the luminescent radiance factor can be factorized into a product of the emission and excitation spectra $D_\mathrm{L}(\lambda_{em}, \lambda_{ex}) = \alpha(\lambda_{em})\beta(\lambda_{ex})$. Since one of the two spectra $\alpha(\lambda_{em})$ and $\beta(\lambda_{ex})$ can be arbitrarily rescaled, we assume that the excitation spectrum is normalized so that $\int_{360}^{700} \beta(\lambda_{ex})d\lambda_{ex} = 1$.

A discrete form of the Donaldson matrix with these properties can be represented as:

$$\mathbf{D} = \mathbf{D}_\mathrm{R} + \mathbf{D}_\mathrm{L} = \begin{bmatrix} \alpha_1\beta_1 & \cdots & \alpha_1\beta_{m-n} & & s_1 & 0 & \cdots & 0 \\ \alpha_2\beta_1 & & \alpha_2\beta_{m-n} & \alpha_2\beta_{m-n+1} & s_2 & & \ddots & \vdots \\ \vdots & & \vdots & \vdots & \ddots & & \ddots & 0 \\ \alpha_n\beta_1 & \cdots & \alpha_n\beta_{m-n} & \alpha_n\beta_{m-n+1} & \cdots & & \alpha_n\beta_{m-1} & s_n \end{bmatrix} \quad (1)$$

where s_i $(i = 1, 2, \ldots, n)$, α_i $(i = 1, 2, \ldots, n)$ and β_i $(i = 1, 2, \ldots, m-1)$ denote the discrete samples of reflectance, emission, and excitation, respectively. The norm of the excitation vector β is normalized as $\|\beta\| = 1$:

$$\sqrt{\sum_{i=1}^{m-1} \beta_i^2} = 1. \quad (2)$$

In this study, we sample the spectral functions at equal wavelength intervals of 5 nm; thus, the Donaldson matrix is described by $m = 69$ and $n = 61$. Figure 2 shows the Donaldson matrix for the left red wall of the Cornell Box in Figure 1. Notably, the hump in the emission wavelength range of 600–700 nm indicates the presence of luminescent radiation factors that produce an orange color.

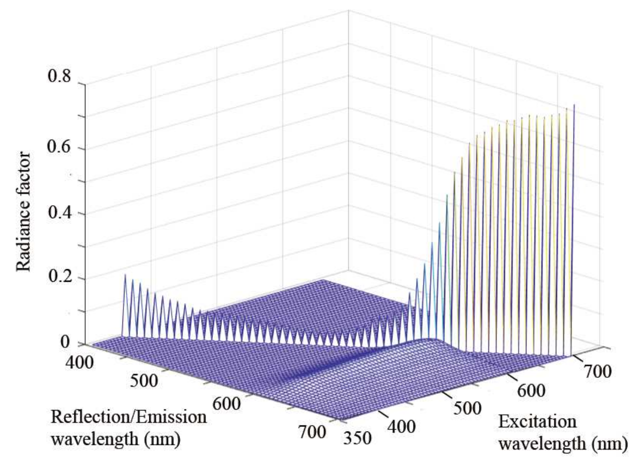

Figure 2: Donaldson matrix for the left red wall of the Cornell Box in Figure 1. The vertical axis indicates spectral radiance factors. Diagonal elements correspond to the surface spectral reflectances producing the red color. Notably, the hump in the emission range of 600–700 nm indicates the presence of luminescent radiance factors that produce an orange color.

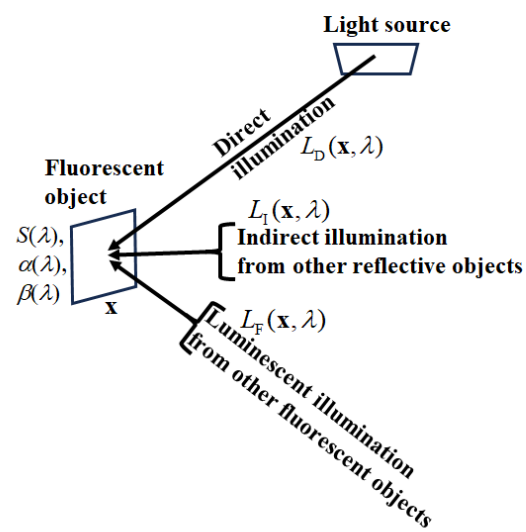

Figure 3: Classification of illumination into three types.

IV. Image formation models

A. Single fluorescent object model

For a matte fluorescent object, the spectral radiance at position $\mathbf{x} = (x, y, z)$ under a single illuminant $L(\lambda)$ can be expressed as a continuous function of the wavelength λ:

$$\begin{aligned} y(\mathbf{x}, \lambda_{em}) &= f_\mathrm{ref}(\mathbf{x}) S(\lambda_{em}) L(\lambda_{em}) \\ &\quad + f_\mathrm{lum}(\mathbf{x})\, \alpha(\lambda_{em}) \int_{360}^{\lambda_{em}} \beta(\lambda_{ex}) L(\lambda_{ex})\, d\lambda_{ex}, \end{aligned} \quad (3)$$

where the first term on the right-hand side represents the reflected radiance and the second term the luminescent radiance. Here, $f_\mathrm{ref}(\mathbf{x})$ and $f_\mathrm{lum}(\mathbf{x})$ denote the shading terms for reflection and luminescence, respectively. In practice, this continuous formulation is discretized as follows:

$$y_i(\mathbf{x}) = f_\mathrm{ref}(\mathbf{x}) s_i L_i + f_\mathrm{lum}(\mathbf{x}) \alpha_i \sum_{j=1}^{i} \beta_j L_j, \qquad (i = 1, 2, \ldots, n). \quad (4)$$

B. Multiple fluorescent object model

Now consider a general environment in which a fluorescent object is surrounded by both fluorescent and non-fluorescent objects, all with matte surfaces. Focusing on the illumination incident on the target fluorescent object, we categorize it into three types (see Figure 3):

1) direct illumination L_D from a light source,
2) indirect illumination L_I reflected from other reflective surfaces,
3) luminescent illumination L_F emitted from surrounding fluorescent surfaces.

Since both light reflection and fluorescent emission occur at the object's surface, the observed spectral radiance for each illumination type is decomposed into reflection and luminescent components as follows:

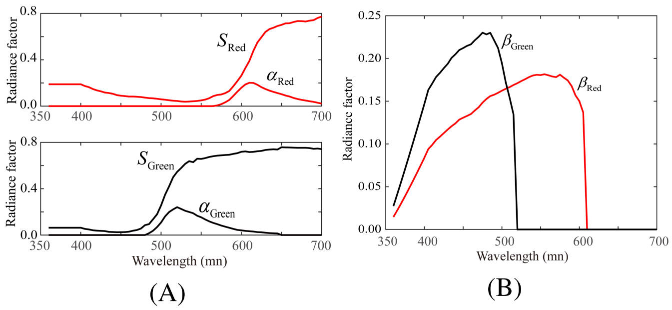

Figure 4: Spectral functions of the spectral reflectance $S(\lambda)$ and emission spectrum $\alpha(\lambda)$ (A), and the excitation spectrum $\beta(\lambda)$ (B), for the two fluorescent walls located on the left and right sides in the Cornell Box in Figure 1.These functions were estimated from real fluorescent sheets [5].

$$\begin{aligned} y(\mathbf{x},\lambda_{em}) &= y_{\text{D,ref}}(\mathbf{x},\lambda_{em}) + y_{\text{D,lum}}(\mathbf{x},\lambda_{em}) \\ &\quad + y_{\text{I,ref}}(\mathbf{x},\lambda_{em}) + y_{\text{I,lum}}(\mathbf{x},\lambda_{em}) \\ &\quad + y_{\text{F,ref}}(\mathbf{x},\lambda_{em}) + y_{\text{F,lum}}(\mathbf{x},\lambda_{em}), \end{aligned} \tag{5}$$

where the components are defined as follows:

- $<1>$ Reflection due to direct illumination from the light source, $y_{\text{D,ref}}$.
- $<2>$ Luminescence due to direct illumination from the light source, $y_{\text{D,lum}}$.
- $<3>$ Reflection due to indirect illumination, $y_{\text{I,ref}}$.
- $<4>$ Luminescence due to indirect illumination, $y_{\text{I,lum}}$.
- $<5>$ Reflection due to luminescent illumination, $y_{\text{F,ref}}$.
- $<6>$ Luminescence due to luminescent illumination, $y_{\text{F,lum}}$.

Because fluorescence–where incident light excites a fluorescent object that subsequently emits light at a longer wavelength–is accompanied by rapid energy attenuation, we assume that fluorescence occurs only once. In other words, the luminescent illumination emitted from a fluorescent object does not re-excite other fluorescent objects. Thus, component $<6>$ can be neglected (i.e., $y_{\text{F,lum}} = 0$).

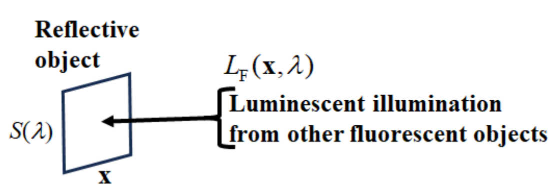

Figure 5: Reflection component $<5>$ due to luminescent illumination emitted from fluorescent objects.

Figure 4 displays the spectral functions of the reflectance $S(\lambda)$, the emission $\alpha(\lambda)$, and the excitation $\beta(\lambda)$ for the two fluorescent walls in the Cornell Box. The luminescent component $<6>$ requires overlap between an excitation spectrum and another material's emission spectrum; under the single-bounce assumption adopted here, we neglect $y_{\text{F,lum}}$ (component $<6>$) and retain only the reflection component $<5>$ for luminescent illumination, as shown in Figure 5. Cases with strong spectral overlap are discussed in Section VIII-A.

To simplify the description of the spectral radiance, we define a combined quantity

$$E(\mathbf{x},\lambda) \triangleq f(\mathbf{x}) L(\mathbf{x},\lambda),$$

which merges the shading term and the illumination. Then, the spectral radiance for each illumination component can be written as follows:

$$\begin{aligned} y_{\text{D,ref}}(\mathbf{x},\lambda_{em}) &= f_{\text{D,ref}}(\mathbf{x}) S(\lambda_{em}) L_{\text{D}}(\mathbf{x},\lambda_{em}) \\ &= S(\lambda_{em}) E_{\text{D,ref}}(\mathbf{x},\lambda_{em}). \end{aligned} \tag{6}$$

$$\begin{aligned} y_{\text{D,lum}}(\mathbf{x},\lambda_{em}) &= f_{\text{D,lum}}(\mathbf{x}) \alpha(\lambda_{em}) \int_{360}^{\lambda_{em}} \beta(\lambda_{ex}) L_{\text{D}}(\mathbf{x},\lambda_{ex})\, d\lambda_{ex} \\ &= \alpha(\lambda_{em}) \int_{360}^{\lambda_{em}} \beta(\lambda_{ex}) E_{\text{D,lum}}(\mathbf{x},\lambda_{ex})\, d\lambda_{ex}. \end{aligned} \tag{7}$$

$$\begin{aligned} y_{\text{I,ref}}(\mathbf{x},\lambda_{em}) &= f_{\text{I,ref}}(\mathbf{x}) S(\lambda_{em}) L_{\text{I}}(\mathbf{x},\lambda_{em}) \\ &= S(\lambda_{em}) E_{\text{I,ref}}(\mathbf{x},\lambda_{em}). \end{aligned} \tag{8}$$

$$\begin{aligned} y_{\text{I,lum}}(\mathbf{x},\lambda_{em}) &= f_{\text{I,lum}}(\mathbf{x}) \alpha(\lambda_{em}) \int_{360}^{\lambda_{em}} \beta(\lambda_{ex}) L_{\text{I}}(\mathbf{x},\lambda_{ex})\, d\lambda_{ex} \\ &= \alpha(\lambda_{em}) \int_{360}^{\lambda_{em}} \beta(\lambda_{ex}) E_{\text{I,lum}}(\mathbf{x},\lambda_{ex})\, d\lambda_{ex}. \end{aligned} \tag{9}$$

$$\begin{aligned} y_{\text{F,ref}}(\mathbf{x},\lambda_{em}) &= f_{\text{F,ref}}(\mathbf{x}) S(\lambda_{em}) L_{\text{F}}(\mathbf{x},\lambda_{em}) \\ &= S(\lambda_{em}) E_{\text{F,ref}}(\mathbf{x},\lambda_{em}). \end{aligned} \tag{10}$$

Assuming Lambertian reflection and (approximately) isotropic fluorescent emission [23], [24], fluorescent emission obeys Lambert's cosine law.

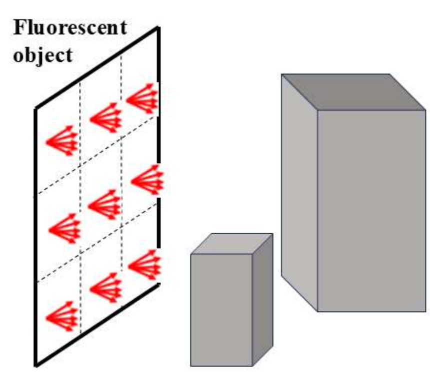

Figure 6: A luminescent object treated as an emitter, with its surface divided into a finite array of subareas where small area lights are spatially arranged.

Therefore, we set $f_{\text{D,ref}}(\mathbf{x}) = f_{\text{D,lum}}(\mathbf{x})$ and $f_{\text{I,ref}}(\mathbf{x}) = f_{\text{I,lum}}(\mathbf{x})$, so the shading terms for the fluorescent components can be obtained from those of the reflection components. As a result, we have $E_{\text{D,ref}}(\mathbf{x},\lambda) = E_{\text{D,lum}}(\mathbf{x},\lambda)$ ($\triangleq E_{\text{D}}(\mathbf{x},\lambda)$) and $E_{\text{I,ref}}(\mathbf{x},\lambda) = E_{\text{I,lum}}(\mathbf{x},\lambda)$ ($\triangleq E_{\text{I}}(\mathbf{x},\lambda)$). The quantity $E(\mathbf{x},\lambda)$ for each illumination can be obtained from the spectral radiance observed from the reflection component for each illumination as follows:

$$\begin{aligned} E_{\mathrm{D}}(\mathbf{x},\lambda_{em}) &= y_{\mathrm{D,ref}}(\mathbf{x},\lambda_{em})\,/\,S(\lambda_{em}), \\ E_{\mathrm{I}}(\mathbf{x},\lambda_{em}) &= y_{\mathrm{I,ref}}(\mathbf{x},\lambda_{em})\,/\,S(\lambda_{em}). \end{aligned} \tag{11}$$

The luminescent components $y_{\mathrm{D,lum}}$ and $y_{\mathrm{I,lum}}$ can then be calculated by substituting $E_{\mathrm{D}}(\mathbf{x},\lambda)$ from Eq. (11) into $E_{\mathrm{D,lum}}(\mathbf{x},\lambda)$ in Eq. (7) and $E_{\mathrm{I}}(\mathbf{x},\lambda)$ into $E_{\mathrm{I,lum}}(\mathbf{x},\lambda)$ in Eq. (9).

Component $< 5 >$ represents the reflection caused by luminescent illumination emitted from another fluorescent object. In this context, the fluorescent object acting as the emitter is treated as a secondary light source that illuminates adjacent reflective surfaces. For rendering, although the spatial distribution of the illuminant intensity is continuous, the emitter's surface is subdivided into a finite number of subareas (see Figure 6), and small area lights are arranged accordingly. The luminescent spectral distribution for each subarea is obtained by spatially averaging the emitted spectrum over that subarea.

C. Reflective object model

For a reflective, non-fluorescent object, only the reflection component contributes to image formation. Thus, the observed spectral radiance is given by:

$$y(\mathbf{x},\lambda_{em}) \;=\; y_{\mathrm{D,ref}}(\mathbf{x},\lambda_{em}) + y_{\mathrm{I,ref}}(\mathbf{x},\lambda_{em}) + y_{\mathrm{F,ref}}(\mathbf{x},\lambda_{em}). \tag{12}$$

V. Component Computation and Renderer Setting

In this study, we employ the non-fluorescent renderer Mitsuba v0.6 [20] to compute the spectral images of scenes containing fluorescent objects. Reflection components are estimated by Monte Carlo simulation (bidirectional path tracing), and luminescent components are computed from the rendered reflection components using Eqs. (7) and (9).

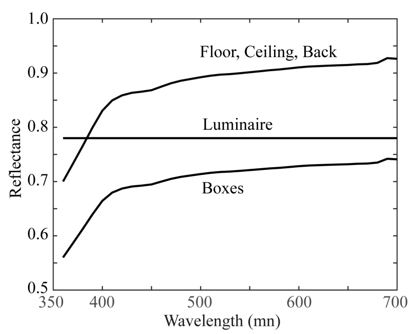

Figure 7: Spectral reflectances for non-fluorescent objects in the Cornell Box.

We use the "bdpt" (bidirectional path tracer) with carefully chosen parameters. The key parameter, "maxDepth", controls the maximum number of bounces in the simulation. For example, setting "maxDepth" to -1 enables infinite bounces to capture full interreflection in the scene, while setting it to 2 limits the simulation to a single reflection from direct illumination. Additionally, the "rrDepth" parameter, defining the minimum path depth at which the Russian roulette termination criterion is applied, is set to 10 to efficiently terminate very long paths. The "independent" sampler is used with 1024 samples per pixel.

The 3D shape data of the objects are imported as OBJ files, and the material BRDF is set to perfect diffuse reflection. A perspective camera model is employed, with its field of view adjusted to ensure the rendered image closely matches photographs of a real Cornell Box. The standard Cornell Box data, including geometry, dimensions, and lighting, were obtained from [19]. In our setup, the left and right walls (red and green, respectively) are treated as fluorescent (Figure 4), while the floor, ceiling, back wall, and two rectangular boxes are matte and non-fluorescent with their spectral reflectances set as shown in Figure 7. The walls are assumed to be standard reference white, and the two boxes are gray. The ceiling light source is modeled after the CIE Standard Illuminant D65, whose spectral power distribution is given in [1], [25], and the lighting luminaire is set to a reflectance of 0.78. Spectral functions (reflectance, excitation, emission, and illuminant spectrum) are sampled at 5 nm intervals over the wavelength range of 360–700 nm.

Each component image is rendered as follows:

$< 1 >$ **Reflection component by direct illumination from a light source,** $y_{\mathrm{D,ref}}(\mathbf{x},\lambda_{em})$

The spectral radiance $y_{\mathrm{D,ref}}(\mathbf{x},\lambda_{em})$ is obtained from the direct-illumination reflection, computed by Mitsuba with "maxDepth = 2"(Figure 8(A)).

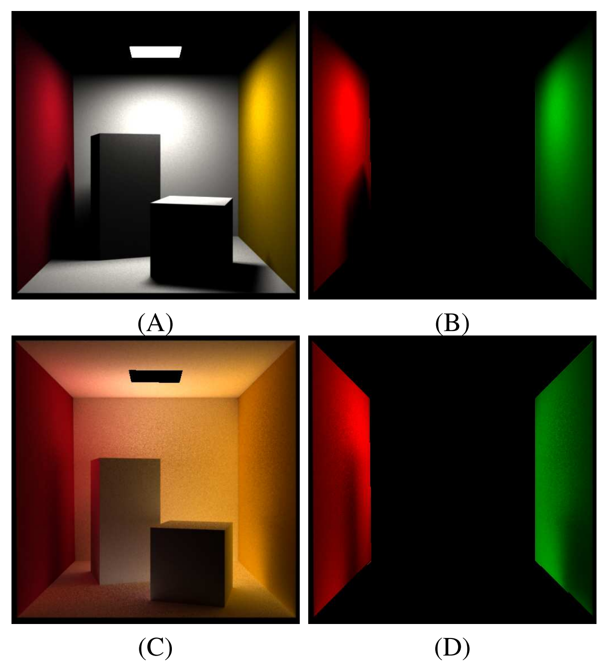

Figure 8: Rendered components $< 1-4 >$: (A) component $< 1 >$; (B) component $< 2 >$; (C) component $< 3 >$; (D) component $< 4 >$.

$< 2 >$ **Luminescence component by direct illumination from a light source,** $y_{\mathrm{D,lum}}(\mathbf{x},\lambda_{em})$

The direct illumination distribution on each object's surface is computed as

$$E_{\mathrm{D}}(\mathbf{x},\lambda_{em}) \;=\; y_{\mathrm{D,ref}}(\mathbf{x},\lambda_{em})\big/S_i(\lambda_{em}),$$

using the spectral reflectance $S_i(\lambda_{em})$ for object surface i. The luminescent component is then calculated using Eq. (7). Figure 8(B) shows the rendered image for this component.

$< 3 >$ **Reflection component by indirect illumination,** $y_{\mathrm{I,ref}}(\mathbf{x},\lambda_{em})$

This component is obtained by subtracting the spectral outputs with “maxDepth = 2” from those with “maxDepth = -1” (i.e., infinite bounces). Figure 8(C) shows the rendered image for this component.

$< 4 >$ **Luminescence component by indirect illumination,** $y_{\mathrm{I,lum}}(\mathbf{x}, \lambda_{em})$

The indirect illumination distribution on each object’s surface is calculated as

$$E_{\mathrm{I}}(\mathbf{x}, \lambda_{em}) \ = \ y_{\mathrm{I,ref}}(\mathbf{x}, \lambda_{em}) / S_i(\lambda_{em}),$$

using the spectral reflectance $S_i(\lambda_{em})$ for object surface i. The luminescent component is computed using Eq. (9). Figure 8(D) shows the rendered image for this component.

$< 5 >$ **Reflection by luminescent illumination,** $y_{\mathrm{F,ref}}(\mathbf{x}, \lambda_{em})$

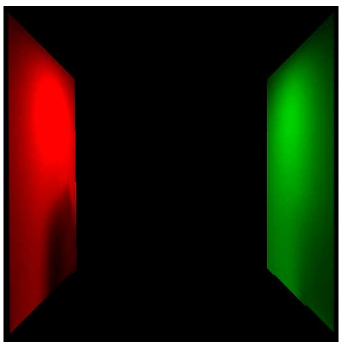

Figure 9: Luminescent image showing light from the left and right walls.

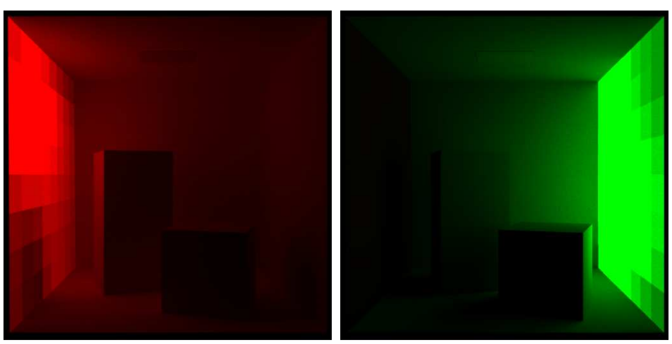

(A) (B)

Figure 10: Rendered images (A) and (B) using 8-by-8 emitters for the left and right fluorescent walls, respectively. The spectral image $y_{\mathrm{F,ref}}(\mathbf{x}, \lambda_{em})$ excludes the fluorescent wall from each spectral image.

The luminescent light $L_{\mathrm{F}}(\mathbf{x}, \lambda_{em})$ from the left and right walls is the sum of the luminescent components from direct and indirect illumination (i.e., components $< 2 >$ and $< 4 >$), shown in Figure 9. Each fluorescent wall is subdivided into an $N \times N$ array of subareas; for each subarea, the luminescent spectral distribution is computed as the spatial average of the emitted spectrum and used to define a diffuse area-light emitter. We render the reflection component $y_{\mathrm{F,ref}}(\mathbf{x}, \lambda_{em})$ for the remaining surfaces with “maxDepth = -1” using this emitter array (Figure 10), excluding the fluorescent wall geometry. Increasing N reduces discretization artifacts but increases rendering time. In our tests, 8×8 provides the best trade-off, while 16×16 yields visually and numerically similar results (between 8×8 and 16×16 the RMSE is 0.0359) at higher cost (Figure 11).

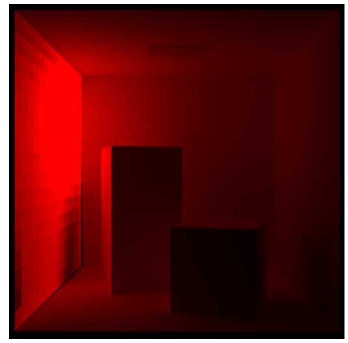

Figure 11: Rendered image with 16×16 emitters for the left fluorescent wall.

(A) (B)

Figure 12: Images based on light reflection only (A) and luminescent illumination only (B).

The overall spectral radiance due to light reflection is $y_{\mathrm{D,ref}}(\mathbf{x}, \lambda_{em}) + y_{\mathrm{I,ref}}(\mathbf{x}, \lambda_{em})$, which is directly obtained from the renderer with “maxDepth = -1”. The spectral radiance from luminescent illumination is the sum $y_{\mathrm{D,lum}}(\mathbf{x}, \lambda_{em}) + y_{\mathrm{I,lum}}(\mathbf{x}, \lambda_{em}) + y_{\mathrm{F,ref}}(\mathbf{x}, \lambda_{em})$. Figures 12(A) and (B) display the images for the reflection and luminescent components, respectively. Finally, the overall spectral radiance is obtained by linearly summing these five components:

$$\begin{aligned} y(\mathbf{x}, \lambda_{em}) \ &= y_{\mathrm{D,ref}}(\mathbf{x}, \lambda_{em}) + y_{\mathrm{D,lum}}(\mathbf{x}, \lambda_{em}) \\ &+ y_{\mathrm{I,ref}}(\mathbf{x}, \lambda_{em}) + y_{\mathrm{I,lum}}(\mathbf{x}, \lambda_{em}) \\ &+ y_{\mathrm{F,ref}}(\mathbf{x}, \lambda_{em}). \end{aligned} \tag{13}$$

This yields the final sRGB image as shown in Figure 1. Figure 13 shows the final sRGB image with 1024-by-1024 pixels.

VI. Experiments

A. Evaluation using a real Cornell Box

A real Cornell Box was constructed with two rectangular objects inside, shown in Figures 14(A) and 14(B). Figure 15 shows the dimensions of the real Cornell Box and the positions and sizes of the objects within it (in mm). The primary construction material for both the box and the objects was wood, with surfaces covered by paper seals. The red and green walls (on the left and right sides of the box, respectively) were

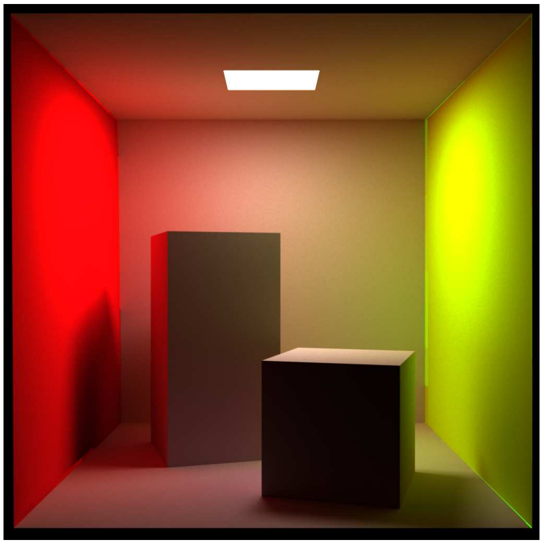

Figure 13: Final sRGB image with 1024-by-1024 pixels.

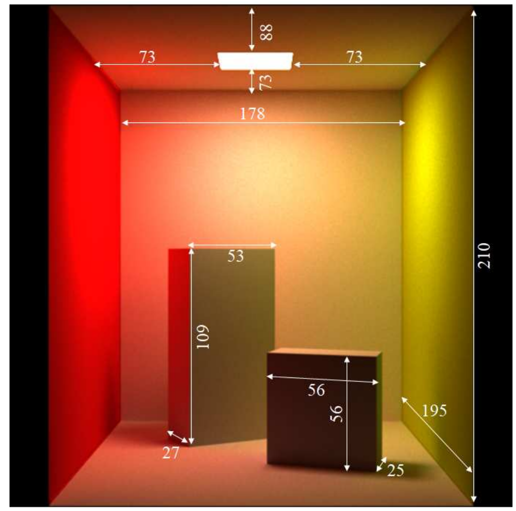

Figure 15: Dimensions of the real Cornell Box and positions/sizes of the objects within it (in mm).

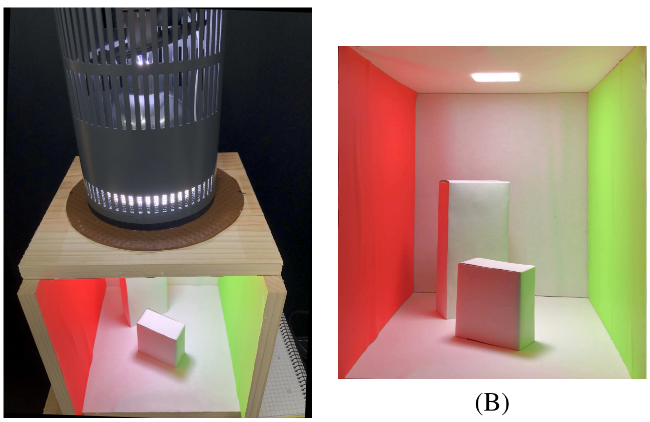

(A) (B)

Figure 14: Real Cornell Box and objects within the box: (A) overview; (B) front view.

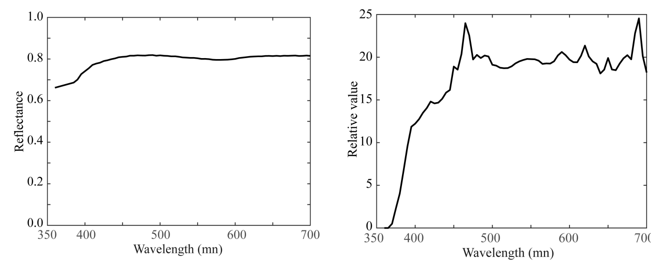

(A) (B)

Figure 16: Spectral functions for reflectance and illuminant power distribution: (A) spectral reflectance of the non-fluorescent white seal used for the ceiling, back, floor, and two rectangular objects; (B) spectral power distribution of an artificial sunlight lamp.

covered with fluorescent paper seals (Lumino Sheet, Okina Inc., Tokyo, Japan), and their surface spectral reflectances along with fluorescence excitation/emission characteristics are displayed in Figure 4(A) and (B). Figure 16(A) and (B) show the spectral functions for reflectance and illuminant power distribution. The ceiling, back, floor, and two small boxes were covered with non-fluorescent white seals (A-one Label Seal, 3M Japan, Tokyo, Japan), and their measured spectral reflectances are shown in Figure 16(A). A hole was cut in the ceiling and covered with a diffuser. The light source, placed at the ceiling hole, is an artificial sunlight lamp (SOLAX 100W, SERIC Ltd., Tokyo, Japan), whose the measured spectral power distribution is shown in Figure 16(B).

Figure 17 shows the rendered sRGB image of the real Cornell Box, derived from the spectral radiance image produced by the Mitsuba renderer using the proposed method. The right green wall in Figure 17 looks slightly different from the image in Figure 1. This is due to the difference in the light sources. The light source in Figure 1 is CIE standard illuminant D65, while the light source in Figure 17 is the artificial sunlight lamp with the spectral power distribution in Figure 16(B).

In the figure, numerical labels indicate the measurement points of the spectral radiance. A spectral radiometer (SpectraScan PR705, Photo Research, USA) with an aperture size of $1/8$ degree was used for these measurements. Figure 18(a) presents a set of spectral distributions sampled at the pixel points corresponding to the numbered measurement points in Figure 17. Figure 18(b) shows a set of spectral radiance distributions directly measured by the spectral radiometer at the same points. The spectral distributions are represented at 5 nm intervals over the visible wavelength range (400–700 nm) and are normalized by the average radiance at the top white surface of the small box numbered 7.

To evaluate the accuracy of the proposed method, the average root-mean-square error (RMSE) was calculated over the 13 spectral distributions $\mathbf{y}_{\text{Proposed}}(\mathbf{x}_i)$ and $\mathbf{y}_{\text{Measured}}(\mathbf{x}_i)$ $(i = 1, 2, \ldots, 13)$ between the generated spectral radiances and the direct measurements, using

$$\mathrm{E}\{\mathrm{RMSE}\} = \left\{ \frac{1}{13} \sum_{i=1}^{13} \left(\frac{1}{61} \left\| \mathbf{y}_{\text{Proposed}}(\mathbf{x}_i) - \mathbf{y}_{\text{Measured}}(\mathbf{x}_i) \right\|^2 \right) \right\}^{1/2}. \tag{14}$$

Additionally, color differences were computed using the CIEDE2000 equation [26]. For this, the spectral distributions

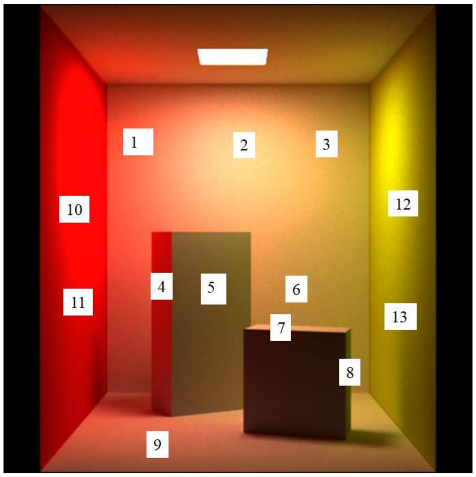

Figure 17: Rendered sRGB image of the real Cornell Box using our method. Numbers indicate measurement points.

were first converted into CIE XYZ tristimulus values and then into CIELAB values, using the spectral radiance measured at point 7 as the white reference. The average values of RMSE and color difference were obtained as $E\{RMSE\} = 0.157$ and $E\{DE_{2000}\} = 2.98$, respectively.

B. Comparison with the other fluorescent renderer

ART [21], [27] is a spectral rendering system that supports fluorescence rendering by allowing the specification of the bispectral characteristics of fluorescent materials. It operates through a suite of specialized tools, including the primary command-line renderer (*artist*) and a tone-mapping utility (*tonemap*). We rendered the Cornell Box using ART with identical scene parameters (geometry, reflectances, illumination, Donaldson matrix from Eq. (1)) for direct comparison with our method.

Figure 19 shows the rendered sRGB image of the real Cornell Box, derived from the spectral radiance image produced by ART. We used ART 2.0.3 here. The SAMPLES option was set to -1 (UNLIMITED), meaning that the sampler continued until manually terminated (approximately 30,000 samples were collected). The internal spectral representation was set with the command-line flag "-s46e", corresponding to a 46-band spectrum with 10 nm intervals over the range of 320–780 nm. For consistency, the ART output spectra were converted from 10 nm to 5 nm intervals via interpolation. Additionally, the average color value on the top white surface (point 7) of the small box was adjusted to match between Figures 17 and 19, and some areas (including the ceiling light source) are saturated (R, G, B > 255). Figure 18(c) shows the set of spectral distributions sampled at the same points as in Figure 17 from the ART output, normalized by the average radiance at the top white surface (point 7).

ART accuracy was evaluated using the same 13 measurement points, yielding $E\{RMSE\} = 0.191$ and $E\{DE_{2000}\} = 6.94$, $E\{RMSE\} = 0.191$ and $E\{DE_{2000}\} = 6.94$, demonstrating that the proposed method achieves substantially higher accuracy than ART.

The processing time cannot be compared between the proposed method and ART. Our method requires simple image processing to extract the fluorescent area in order to render component $< 5 >$, while ART does not require this.

VII. Generalization to Non-planar Fluorescent Objects

To demonstrate generalizability to non-planar geometry, we rendered a fluorescent Stanford Bunny [28] (72,027 vertices, 144,046 triangles) placed inside the Cornell Box. The Cornell Box configuration, materials, camera, and lighting follow Section V.

We suppose that the bunny exhibits white diffuse reflection and orange diffuse fluorescence. Figure 20 shows the spectral functions of the reflectance $S(\lambda)$, the emission $\alpha(\lambda)$, and the excitation $\beta(\lambda)$ for the bunny. The fluorescent spectral functions were obtained from a real fluorescent object (see [5]). Note that the spectral reflectance is assumed to be the same as that of the boxes in the Cornell Box shown in Figure 7. All spectral functions were sampled at 5 nm intervals over the wavelength range of 360–700 nm. The spectrally rendered images have the size of 512-by-512 pixels. Figures 21(A)–(D) display the rendered images in the same manner as in Section V for components $< 1-4 >$.

Next, we consider component $< 5 >$, that is, the reflection component due to luminescent illumination based on the sum of components $< 2 >$ and $< 4 >$. This component is composed of three types of luminescent light from the left wall, the right wall, and the bunny. Fluorescence emitters are analyzed for each fluorescent object individually. The same procedure as previously was applied to the left and right walls. The fluorescent walls were divided into an 8-by-8 grid of subareas. For each subarea, the luminescent spectral distribution was computed as the spatial average of the emitted spectral distribution. The reflection component image for all reflective surfaces in the Cornell Box was spectrally rendered using these 8-by-8 emitters in Mitsuba with `maxDepth` $= -1$. Figures 22(A) and (B) demonstrate the rendered images based on the 8-by-8 emitters for the left and right fluorescent walls, respectively, where the fluorescent walls with emitters were excluded from the rendered images.

Concerning component $< 5 >$ for the bunny, we must consider reflection of objects near the bunny in the Cornell Box. From the camera's viewpoint, there are light-emitting curved objects in front of and behind the bunny. In particular, objects at the back of the box are illuminated by the bunny's fluorescence emission. To estimate the fluorescence emission from the back of the bunny, a camera was placed on the back of the Cornell Box. Figure 23 shows an image rendered with `maxDepth` $= -1$ where the camera was placed on the back wall of the box opposite the current camera position.

A finite number of fluorescent emitters were placed on the bunny. To do this, the bunny is approximated by a finite number of triangular polygons, and emitter primitives were instantiated at the face centroids. Figures 24(A) and (B) show the bunny approximated using a total of 100 polygon faces on the front and back, respectively, where the red square

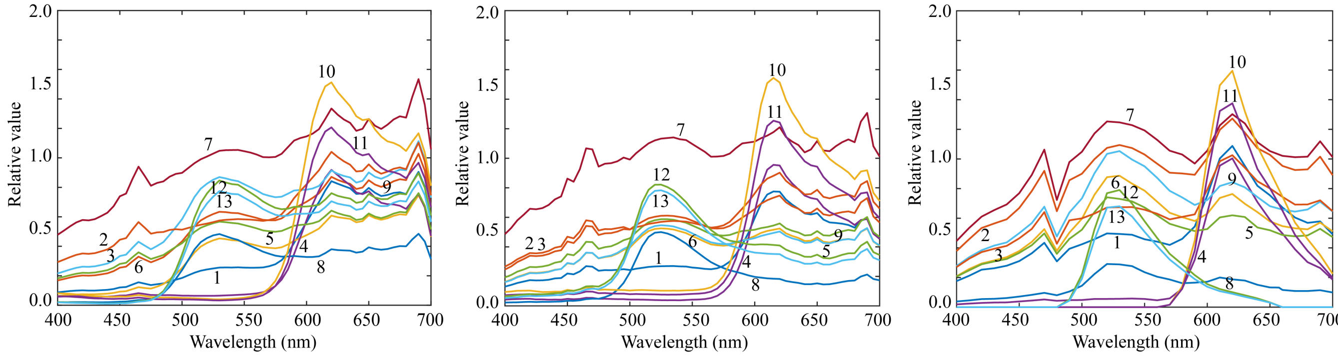

(a): Our method (b): Ground truth (c): ART renderer

Figure 18: In (a), spectral distributions sampled at pixel points corresponding to the numbered measurement points in Figure 17. (b) Spectral radiance distributions directly measured by the spectral radiometer at the same points. (c) Spectral distributions from the ART output sampled at the same measurement points as in Figure 17. In all cases, the curves are normalized by the average radiance at the top white surface of small box 7.

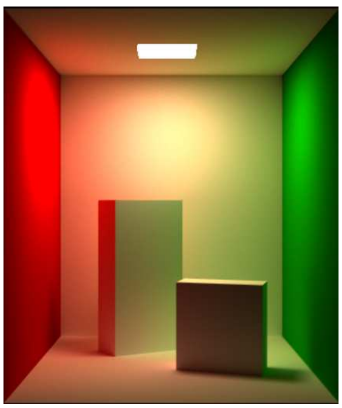

Figure 19: Rendered sRGB image of the real Cornell Box, derived from the spectral radiance image produced by ART.

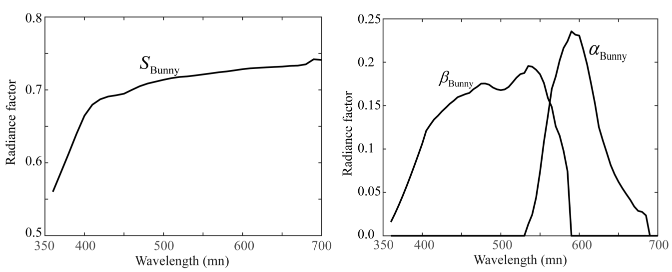

(A) (B)

Figure 20: Spectral functions of the reflectance $S(\lambda)$ (A), the emission spectrum $\alpha(\lambda)$, and the excitation $\beta(\lambda)$ (B) for the bunny.

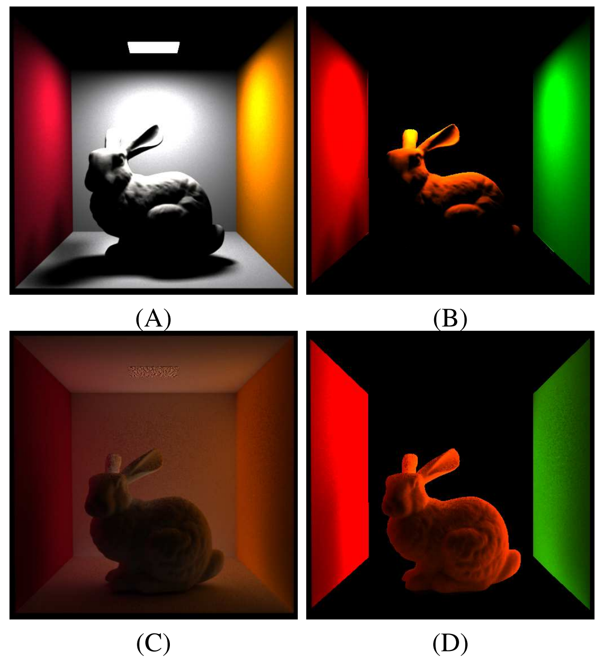

Figure 21: Rendered components $<1-4>$: (A) component $<1>$; (B) component $<2>$; (C) component $<3>$; (D) component $<4>$.

dots represent the center points of the respective triangles. Each emitter has diffuse emission, and the fluorescent spectral power distribution is determined on the image plane. In this paper, we assume a pinhole camera, as shown in Figure 25.

Assuming a pinhole camera, the following relationship holds between the three-dimensional coordinates (X,Y,Z) of a point in space and the coordinates (x,y) on the two-dimensional image, where f is a focal length:

$$x = f\frac{X}{Z}, \qquad y = f\frac{Y}{Z}. \tag{15}$$

Since the geometry of the Cornell Box is known, f is estimated, and the corresponding point on the image for the polygon center that approximates the bunny is found. When the camera is on the back of the bunny, the camera position is close to the object, so the above assumption of a pinhole camera introduces an error. Therefore, a more direct projection model was used, where $\mathbf{P}$ is the 2×3 projection matrix:

$$\begin{bmatrix} x \\ y \end{bmatrix} = \mathbf{P}\begin{bmatrix} X \\ Y \\ Z \end{bmatrix}, \tag{16}$$

The matrix $\mathbf{P}$ is estimated by using the known geometry of the Cornell Box and by extracting some feature points from the bunny surface.

Figure 26 shows the rendered images based on the emitters shown in Figure 24 for the front (A) and back (B). These images demonstrate the reflection effects due to the fluores-

(A) (B)

Figure 22: Rendered images based on the wall emitters (8-by-8 subdivision) for the left (A) and right (B) fluorescent walls.

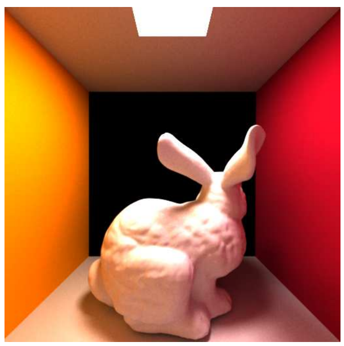

Figure 23: Rendered image with `maxDepth`$=-1$ and the camera placed on the back wall of the box.

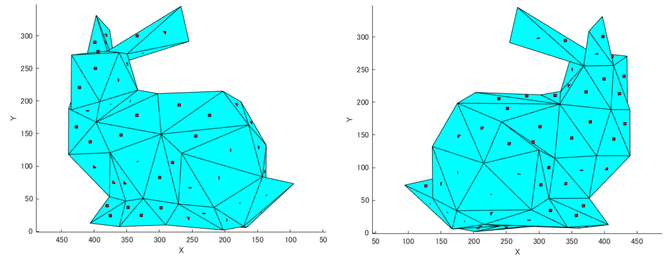

(A) (B)

Figure 24: Bunny approximated using a total of 100 polygon faces on the front (A) and back (B), where the red square dots represent the centers of the respective triangles.

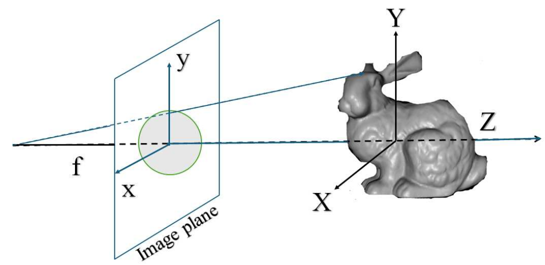

Figure 25: Setup of a pinhole camera.

cence emission from the front and back of the bunny. Note that the reflection effects at the back are much stronger than on the front side. The rendered image for component $< 5 >$ combines all reflection effects due to the three fluorescent objects: the left wall, the right wall, and the bunny.

Finally, the overall spectral radiance was obtained by linearly summing the five components. Figure 27 displays the final RGB image.

Rendering times. Spectral images (512×512 pixels, 69 wavelength bands at 5 nm intervals in the range 360-700 nm) were rendered using Mitsuba with the following relative times:

- 1.00: Direct reflection (component $< 1 >$);
- 6.11: Infinite-bounce reflection;
- 3.52: Reflection from left wall luminescence;
- 3.52: Reflection from right wall luminescence;
- 2.04: Reflection from bunny front luminescence;
- 3.80: Reflection from bunny rear luminescence.

Total wall-clock time was 24 minutes (consumer laptop—Panasonic CF-SC). Post-processing components $< 2, 4, 5 >$ and RGB conversion in MATLAB added negligible overhead.

Comparison with ART. Figure 28 shows a side-by-side comparison of sRGB images between two resulting images using the proposed method and the ART method, where both images were transformed so that their overall average luminance values matched. Figure 29 shows a difference map between the two images, where the difference image for each RGB component was calculated to produce a color image.

Note that the color difference of the ceiling lighting is large. ART internally provides the D65 spectral distribution at 10 nm intervals, while we used the D65 spectral distribution specified by CIE at 5 nm intervals in our method. While color differences in the bunny region are modest, differences on the fluorescent right wall are significant.

VIII. Conclusions

We proposed a spectral rendering method for fluorescent objects using a non-fluorescent renderer. We demonstrated that general environments—where a fluorescent object is surrounded by both fluorescent and non-fluorescent objects with matte surfaces—can be effectively simulated, as illustrated using a Cornell Box setup containing fluorescent objects.

Our method decomposes incident illumination on fluorescent surfaces into three types: (1) direct from light sources, (2) indirect from reflective objects, and (3) luminescent from other fluorescent objects. Each type is further decomposed into reflection and luminescence components. Assuming single-bounce fluorescence and isotropic emission (similar to Lambertian reflection), we express the total spectral radiance as a linear combination of five components, with fluorescent shading terms derived from their reflection counterparts. The fifth component treats luminescent objects as secondary area-light sources.

We implemented this decomposition in Mitsuba V0.6, a conventional spectral renderer. We described the practical computational procedure and parameter settings for each component, with spectral functions (reflectance, excitation, emission, and illuminant) sampled at 5 nm intervals over the wavelength range of 360–700 nm. Image resolutions were 512×512 and 1024×1024 pixels; post-processing was performed in MATLAB.

Experimental validation using a physical Cornell Box demonstrated accuracy via RMSE and CIEDE2000 metrics

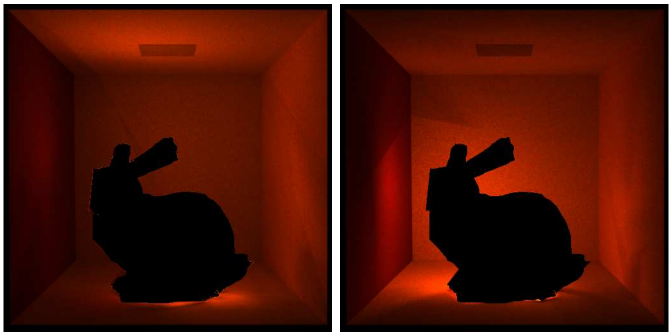

(A) (B)

Figure 26: Rendered images based on the emitters shown in Figure 24 for the front (A) and back (B).

Figure 27: Final RGB image from linearly summing the five components.

compared to direct spectroradiometric measurements. Comparison with ART, a native fluorescence renderer, showed our method achieves substantially higher accuracy (RMSE: 0.157 vs. 0.191; ΔE_{2000}: 2.98 vs. 6.94) despite the simplifying assumptions.

Finally, we demonstrated generalization to non-planar fluorescent objects using a Stanford Bunny model. Overall, the results confirm that conventional renderers can be effectively adapted for accurate spectral rendering of fluorescent scenes, offering a practical solution for broader applications.

A. Limitations and extensions

Single-bounce fluorescence. Our model assumes *single-bounce* fluorescence between fluorescent objects; scenes with strong re-excitation (i.e., substantial overlap between the excitation spectrum β of one surface and the emission spectrum α of another across multiple materials) are out of scope. Extending the approach to controlled multi-bounce cases is conceptually straightforward but would require estimating additional luminescence terms (e.g., iterating the mutual-illumination computation).

Purely diffuse (Lambertian) surfaces. We assume matte reflection and approximately isotropic fluorescent emission. Specular or glossy fluorescent materials (e.g., coated plastics

(A) (B)

Figure 28: Side-by-side comparison of sRGB images between the proposed method (A) and ART (B), where both images were transformed so that their overall average luminance values matched.

Figure 29: RGB difference map between our method and ART (Figure 28).

or gemstones such as diamonds) are out of scope because their directionally varying appearance cannot be recovered from diffuse shading terms alone; such cases would require directional measurements (BBRRDFs) and corresponding evaluation in the renderer.

Donaldson matrix measurements. Our method requires a Donaldson matrix (or its factorization) and reflectance spectra for each fluorescent material. These quantities are typically measured or estimated from multispectral data; noise and model mismatch propagate directly to the rendered spectra, and materials with multiple fluorophores may require higher-rank (or full) bispectral representations.

Emitter discretization and non-planar objects. Component $< 5 >$ approximates luminescent illumination by subdividing fluorescent surfaces into a finite set of diffuse area-light emitters. Coarse subdivisions can introduce artifacts, while finer subdivisions increase rendering time (Section V). For non-planar objects, emitter placement is currently manual; automation via adaptive subdivision or contribution-driven sampling would be a natural extension.

Edge artifacts and geometric precision. At corners where white and fluorescent plates meet, enhanced fluorescent emission can occur due to strong local reflection. Additionally, geometric discretization at sharp edges can produce localized bright artifacts. These effects are sensitive to floating-point precision in geometry placement; even microscopic misalignments can create extremely small distances causing numerical instabilities in geometric terms. We addressed these through spatial filtering; more robust solutions (e.g., distance clamping, higher-precision geometry, or adaptive near-field sampling) could be explored in future work.

Spectral range. The excitation range in our Mitsuba configuration is limited to 360–700 nm; materials primarily excited below 360 nm would require extending the renderer and measurements into the UV.

Acknowledgments

This work was supported by Japan Society for the Promotion of Science Grant Number JP24K15014. The authors thank Prof. Kosuke Mochizuki (Nagano University) for help in creating the emitter array in Blender, Ms. Eriko Tominaga for help with software implementation, and Ms. Rinko Tominaga for help with experiments using a real Cornell Box.

References

[1] G. Wyszecki and W. S. Stiles, *Color Science: Concepts and Methods, Quantitative Data and Formulae*, 2nd ed. New York, NY, USA: Wiley-Interscience, 2000.

[2] J. R. Lakowicz, *Principles of Fluorescence Spectroscopy*, 3rd ed. Berlin, Germany: Springer, 2006.

[3] R. Donaldson, "Spectrophotometry of fluorescent pigments," *Br. J. Appl. Phys.*, vol. 5, no. 6, pp. 210–214, 1954.

[4] M. B. Hullin, J. Hankika, B. Ajdin, H. P. Seidel, J. Kautz, and H. P. A. Lensch, "Acquisition and analysis of bispectral bidirectional reflectance and reradiation distribution functions," *ACM Trans. Graphics*, vol. 29, no. 4, pp. 1–7, 2010. DOI: 10.1145/1778765.1778834.

[5] S. Tominaga, K. Hirai, and T. Horiuchi, "Estimation of bispectral Donaldson matrices of fluorescent objects by using two illuminant projections," *J. Opt. Soc. Am. A*, vol. 32, no. 6, pp. 1068–1078, 2015.

[6] S. Tominaga, K. Hirai, and T. Horiuchi, "Estimation of fluorescent Donaldson matrices using a spectral imaging system," *Opt. Express*, vol. 26, no. 2, pp. 2132–2148, 2018.

[7] S. Tominaga, "Estimation of bispectral characteristics of fluorescent objects based on multispectral imaging data," *Opt. Eng.*, vol. 60, no. 3, Art. no. 033102, 2021. DOI: 10.1117/1.OE.60.3.033102.

[8] Q. Hua, V. Tazlar, A. Fichet, and A. Wilkie, "Efficient storage and importance sampling for fluorescent reflectance," *Comput. Graphics Forum*, vol. 42, no. 1, pp. 47–59, 2023.

[9] T. Iser, L. Lachiver, and A. Wilkie, "Affordable method for measuring fluorescence using Gaussian distributions and bounded MESE," *Opt. Express*, vol. 31, no. 15, pp. 24347–24362, 2023. DOI: 10.1364/OE.495459.

[10] A. Wilkie, R. Tobler, and W. Purgathofer, "Combined rendering of polarization and fluorescence effects," in *Rendering Techniques 2001*, S. J. Gortler and K. Myszkowski, Eds. Vienna: Springer, 2001, pp. 197–204.

[11] A. Wilkie, A. Weidlich, C. Larboulette, and W. Purgathofer, "A reflectance model for diffuse fluorescent surfaces," *Proc. Graphite*, pp. 321–328, 2006.

[12] A. Jung, J. Hamika, S. Marschner, and C. Dachsbacher, "A simple diffuse fluorescent BBRRDF model," *Proc. Workshop Material Appearance Modeling*, Eurographics Association, pp. 15–18, 2018.

[13] M. Mojzík, A. Fichet, and A. Wilkie, "Handling fluorescence in a unidirectional spectral path tracer," *Comput. Graphics Forum*, vol. 37, no. 4, pp. 77–94, 2018.

[14] A. Jung, J. Hamika, and C. Dachsbacher, "Spectral mollification for bidirectional fluorescence," *Comput. Graphics Forum*, vol. 39, no. 2, pp. 373–384, 2020.

[15] S. Tominaga and G. C. Guarnera, "Appearance synthesis of fluorescent objects with mutual illumination effects," *Color Res. Appl.*, vol. 47, no. 3, pp. 615–629, 2022. DOI: 10.1002/col.22747.

[16] C. M. Goral, K. E. Torrance, D. P. Greenberg, and B. Battaile, "Modeling the interaction of light between diffuse surfaces," *SIGGRAPH Comput. Graph.*, vol. 18, no. 3, pp. 213–222, 1984.

[17] G. W. Meyer, H. E. Rushmeier, M. F. Cohen, D. P. Greenberg, and K. E. Torrance, "An experimental evaluation of computer graphics imagery," *ACM Trans. Graph.*, vol. 5, no. 1, pp. 30–50, 1986.

[18] Z. Lyu *et al.*, "Validation of image systems simulation technology using a Cornell Box," *Proc. IS&T Int'l. Symp. Electron. Imaging: Imaging Sensors Syst.*, pp. 122-1–122-7, 2021. DOI: 10.2352/ISSN.2470-1173.2021.7.ISS-122.

[19] "Cornell Box data." [Online]. Available: https://www.graphics.cornell.edu/online/box/data.html

[20] W. Jakob, "Mitsuba renderer," 2014. [Online]. Available: https://www.mitsuba-renderer.org/

[21] ART Development Team, ART Renderer. [Online]. Available: https://cgg.mff.cuni.cz/ART/download/

[22] M. Mohammadi, "Developing an imaging bi-spectrometer for fluorescent materials," Ph.D. dissertation, Chester F. Carlson Center for Imaging Science, Rochester Institute of Technology, Rochester, NY, 2009.

[23] T. Treibitz, Z. Murez, B. G. Mitchell, and D. Kriegman, "Shape from fluorescence," in *Proc. European Conference on Computer Vision (ECCV)*, Berlin, Heidelberg: Springer, 2012, Lecture Notes in Computer Science, vol. 7578, pp. 292–306.

[24] S. Tominaga, K. Hirai, and T. Horiuchi, "Measurement and modeling of bidirectional characteristics of fluorescent objects," in *Proc. 16th International Symposium on Multispectral Colour Science*, LNCS 8509, New York: Springer-Verlag, 2014, pp. 35–42.

[25] R. W. G. Hunt and M. R. Pointer, *Measuring Colour*, 4th ed. New York, NY, USA: Wiley, 2011.

[26] G. Sharma, W. Wu, and E. N. Dalal, "The CIEDE2000 color-difference formula: Implementation notes, supplementary test data, and mathematical observations," *Color Res. Appl.*, vol. 30, no. 1, pp. 21–30, 2005.

[27] ART Development Team, *ART Renderer*. [Online]. Available: https://gitlab.com/art-development-team/ART/ (Accessed: Mar. 2024).

[28] Stanford Team, *Stanford Bunny data*. [Online]. Available: https://graphics.stanford.edu/data/3Dscanrep/ (Accessed: July 2025).

[29] S. Tominaga, K. Kato, K. Hirai, and T. Horiuchi, "Spectral image analysis of mutual illumination between florescent objects," *J. Opt. Soc. Am. A*, vol. 33, no. 8, pp. 1476-1487, 2016.

Shoji Tominaga received the Ph.D. degrees from Osaka University, Japan, in 1975. In 2006, he joined Chiba University, Japan, where he was a Professor (2006-2013) , Dean (2011-2013) , a Specially Appointed Researcher (2013-2018) at Graduate School of Advanced Integration Science. He is an adjunct Professor at NTNU, Norway. His research interests include multispectral imaging and material appearance. He is Life Fellow IEEE, Fellow IST, Life Fellow SPIE, and Fellow OSA.

Giuseppe Claudio Guarnera received his Ph.D. from the University of Catania, Italy, in 2013. He is currently an Associate Professor at the University of York, UK, and the Chief Scientific Officer at Lumirithmic Ltd. His research interests include material and facial appearance acquisition, perception, and rendering. He has gained experience across academia and industry at institutions including the University of Southern California, the University of Milano-Bicocca, NTNU, and the University of Giessen.

Ryo Ohtera received his Ph.D. degree from Chiba University, Japan, in 2010. In the same year, he joined the Kobe Institute of Computing, Graduate School of Information Technology, Japan, where he served as an Assistant Professor (2010–2017), Senior Lecturer (2017–2020), and Associate Professor (2020–2025). He is currently a Professor at the Kobe Institute of Computing, Graduate School of Information Technology.